Available online at www.sciencedirect.com
SCIENCE DIRECT®
Journal of Nuclear Materials 328 (2004) 115–123
journal of nuclear materials
www.elsevier.com/locate/jnucmat

Cyclic cracking behavior of low-alloy pressure vessel steel in simulated BWR water

X. Wu *, Y. Katada

Corrosion Resistant Design Group, Steel Research Center, National Institute for Materials Science, 1-2-1 Sengen, Tsukuba, Ibaraki 305-0047, Japan

Received 3 July 2003; accepted 18 March 2004

Abstract

Fatigue crack initiation and growth behavior of low-alloy pressure vessel steel A533B has been investigated in simulated BWR water. Two distinguished crack morphologies were observed, closely depending on the cyclic strain rate. At a high strain rate, fatigue cracks grew in a tortuous manner. Final failure pre-dominantly resulted from the continuous growth of a single fatigue crack. A rough fracture surface was obtained on which hydrogen-induced cracking features were dominant. At a low strain rate, however, fatigue cracks developed in an entirely straight manner. Final failure was usually caused by the joint development of multi-site fatigue cracks. A flat fracture surface was obtained on which slight crack arrest rather than typical hydrogen-induced cracking feature was found. In addition, apparent acceleration in fatigue crack growth rate was observed in the temperature and strain-rate regions of dynamic strain aging (DSA). Related environmentally assisted cracking (EAC) mechanisms are also discussed.

1. Introduction

Corrosion fatigue cracking has been shown to be one of the most significant corrosion-involved phenomena in light water reactor plants, especially for the pressure boundary components [1]. Understanding of the related environmentally assisted cracking (EAC) mechanisms and prevention of the corrosion-involved cracking in high-temperature water environments are therefore issues of considerable significance for these safety-related pressure vessels and piping. Although great number of data have been piled up to evaluate the fatigue crack initiation and growth resistance of pressure vessel steels in high-temperature water environments during past several decades [2–15], some debates still remain on this area, especially for the underlying EAC mechanisms involved. Detailed examination of cracking and fractographic features is well known to assist the in-depth understanding of service failures and the related mechanisms in corrosive environments, due to offering relatively direct evidence to disclose material, mechanical and environmental effects involved. In present work, the fatigue crack initiation and growth behavior of a low-alloy pressure vessel steel A533B has been investigated in simulated BWR water. Main attention was paid to the cyclic cracking and fractographic features. It is expected to clarify the relationships between typical cracking/fractographic features and related mechanisms, and in turn to advance the understanding of the EAC mechanisms of pressure vessel steels in high-temperature water environments.

2. Experimental

The A533B rolled plate was used in the present work, whose chemical compositions, mechanical properties at room temperature are listed in Table 1. The as-received material had been austenized at 1173 K for 3 h and

* Corresponding author. Tel.: +81-29 859 2161; fax: +81-29 859 2101.
E-mail address: wu.xinqiang@nims.go.jp (X. Wu).

0022-3115/$ - see front matter © 2004 Elsevier B.V. All rights reserved.
doi:10.1016/j.jnucmat.2004.03.004

Table 1
Chemical compositions (wt%) and mechanical properties of A533 B steel used presently

C	Si	Mn	P	S	Ni	Cr	Cu	Co	Mo	V	Al	N	O	Fe	Yield strength (MPa)	Ultimate strength (MPa)	Elongation (%)	Reduction in area (%)
0.17	0.25	1.39	0.003	0.013	0.59	0.004	<0.005	0.007	0.46	<0.003	0.026	36[a]	<10[a]	Bal.	461	584	23.5	58

[a] Ppm.

water quenched, then tempered at 933 K for 3 h followed by air cooling, and then annealed at 873 K for 25 h to relieve the stress. Inclusions were frequently observed along the rolling direction on the polished surfaces (Fig. 1(a)). Energy dispersive X-ray spectrometry (EDX) indicated that most of the inclusions were MnS with elongated rod-like morphology from less than 1 μm to more than 50 μm in length. The as-received microstructure is typical upper bainite having well-developed laths (Fig. 1(b)), in which the precipitated carbides are mainly M_3C with size of about 0.1–1 μm (Fig. 1(c)).

Cylindrical specimens with 8 mm in gauge diameter and 16 mm in gauge length were used for low cycle fatigue (LCF) tests. Compact tension type (1TCT) specimens in the L–S orientation of 50 mm width and 25 mm thickness were employed for fatigue crack growth (FCG) tests. Pre-cracking was performed in ambient air. The testing installations were similar to those used in the previous studies [3,6]. The LCF life, N_{25} was defined as a number of cycles at which the peak tensile stress descended to 75% of the level of the maximum peak stress. The test conditions and simulated BWR water chemistry are summarized in Table 2.

The fatigue crack morphologies on specimen surfaces and longitudinal sections were carefully examined using a scanning electron microscope (SEM) equipped with an EDX. The surface crack number in specimen gauge length was counted. Some tested specimens were broken up in liquid nitrogen and the corresponding fracture surfaces were observed.

3. Results

3.1. LCF behavior

Fig. 2 shows *S–N* curves of A533B steel in simulated BWR water. The LCF resistance of the steel was susceptible to the strain rate. More remarkable environmental effects appeared at lower strain rates. Fig. 3 shows the strain-rate response of the peak tensile stress difference $\Delta\sigma_p$. Here $\Delta\sigma_p$ denotes the gap between the stabilized peak tensile stress at strain rate of $0.1\%\,s^{-1}$ and those at other strain rates. An anomalous strain-rate response was observed for the $\Delta\sigma_p$. A maximum $\Delta\sigma_p$ appeared at a strain rate of approximate $0.01\%\,s^{-1}$. Moreover, such maximum $\Delta\sigma_p$ became more remarkable with increasing strain range. This indicated that the dynamic strain aging (DSA) played a certain role in the corrosion fatigue process of A533B steel in simulated BWR water.

Fig. 4 shows typical macromorphologies of specimens tested in simulated BWR water. It was found that surface crack morphologies changed remarkably with decrease of the strain rate. At relatively high strain rate ($0.1\%\,s^{-1}$), the fatigue crack grew in a tortuous manner.

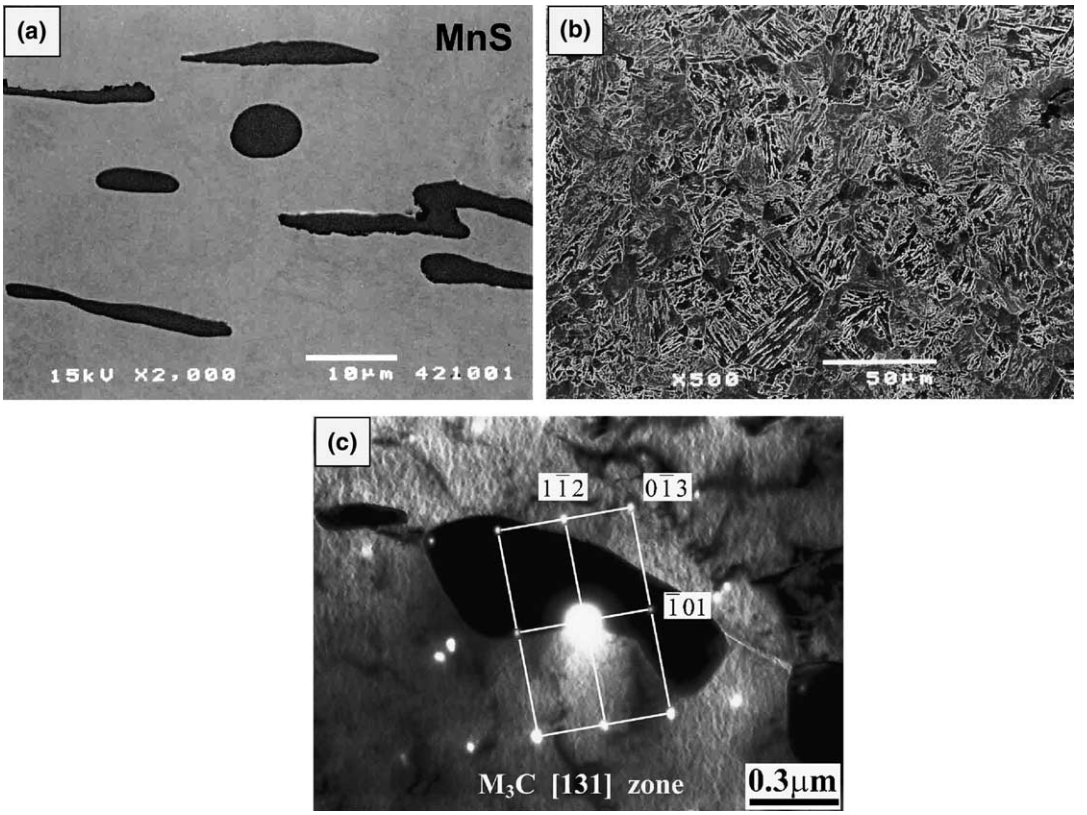

Fig. 1. Inclusion and microstructure morphologies of A533B steel used presently: (a) MnS inclusions, (b) upper bainite and (c) precipitated carbides.

Table 2
Test conditions and simulated BWR water chemistry

LCF tests		FCG tests	
Control mode	Strain	Control mode	Load
Wave form	Triangle	Wave form	Sinusoidal
Strain rate	0.001, 0.01, 0.1% s^{-1}	Frequency	0.0167 Hz
Strain range	0.6–1.5%	Stress ratio	0.1
Temperature	561 K	Temperature	448–593 K
Pressure	8.0 MPa	Pressure	8.0 MPa
Water chemistry		Water chemistry	
Dissolved oxygen	0.1 ppm	Dissolved oxygen	0.1 ppm
pH	6.2–6.5	pH	6.2–6.5
Conductivity	<0.2 μS/cm	Conductivity	<0.2 μS/cm

The final failure predominantly resulted from the continuous growth of a single fatigue crack (Fig. 4(a)). At low strain rate (0.001% s^{-1}), however, the fatigue crack developed in an entirely straight manner. The final failure was usually caused by the joint development of multi-site fatigue cracks (Fig. 4(b)).

Fig. 5(a) shows the relationship between surface crack density d_c and cyclic strain rate. Here d_c (mm^{-2}) is defined as the ratio between the surface crack number N_s in gauge length and surface area S_s (mm^2) in gauge length of a specimen, i.e., $d_c = N_s/S_s$. The d_c increased with the decrease of strain rate, which indicated that the resistance of the steel to fatigue crack initiation in high temperature water was susceptible to the cyclic strain rate. The lower the cyclic strain rate, the lower the resistance to fatigue crack initiation. Fig. 5(b) shows the dependence of d_c on total cyclic tensile time t_t (h), which is defined as the product of the rise time t_r (h) in a

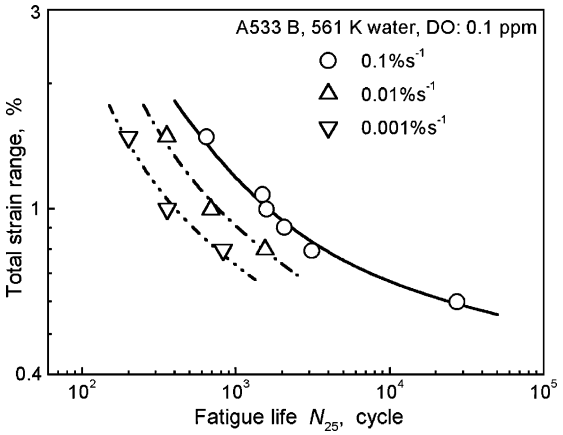

Fig. 2. *S–N* curves for A533B steel in simulated BWR water.

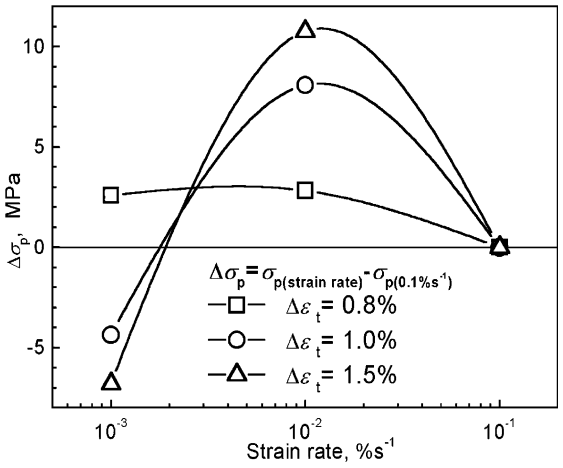

Fig. 3. Strain-rate response for the peak tensile stress difference.

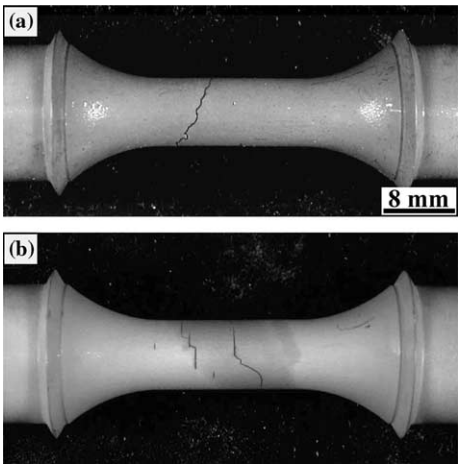

Fig. 4. Macroscopic surface morphologies of specimens after LCF (0.8% strain range) in simulated BWR water at strain rate of (a) $0.1\%\,s^{-1}$ and (b) $0.001\%\,s^{-1}$.

loading cycle and total cycle number N_{25} i.e., $t_t = t_r \times N_{25}$ The fatigue crack initiation resistance in simulated BWR water was also associated with the cyclic tensile time. The d_c and t_t approximately obeyed a power-law relationship

$$d_c = d_0 + k_d \cdot t_t^{0.5}, \quad (1)$$

where d_0 and k_d were fitting coefficients with values of $0.01313\ mm^{-2}$ and $0.1133\ mm^{-2}\,h^{-0.5}$.

Fig. 6 shows typical fatigue crack morphologies on the longitudinal sections. Similarly, a tortuous cracking feature was observed for the case of high strain rate (Fig. 6(a)), while relatively straight inward cracks (both main and secondary) were found for the case of low strain rate (Fig. 6(b) and (c)). Fig. 7 shows typical fracture surface morphologies. At high strain rate, a quite rough fracture surface was obtained (Fig. 7(a)), on which typical

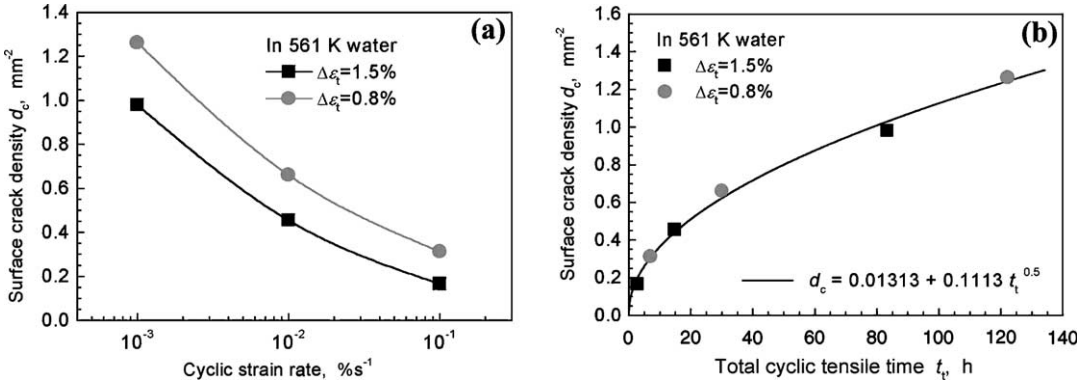

Fig. 5. Relationships between surface crack density in gauge length and cyclic strain rate (a) and total cyclic tensile time (b) in simulated BWR water.

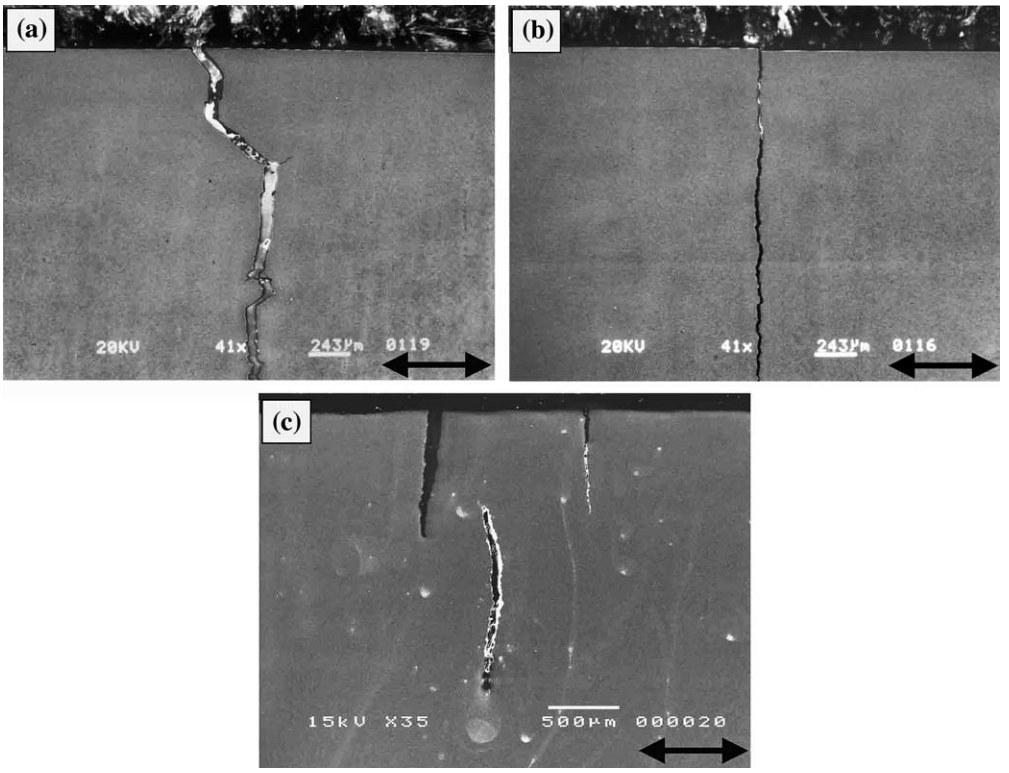

Fig. 6. Typical crack morphologies on longitudinal sections of specimens after LCF (0.8% strain range) in simulated BWR water at different strain rates (arrows: loading direction): (a) $0.1\%\,s^{-1}$, main crack, (b) $0.001\%\,s^{-1}$, main crack, (c) $0.001\%\,s^{-1}$, secondary cracks.

hydrogen-induced cracking features, such as quasi-cleavage patterns and terraced morphology (Fig. 7(c)), were dominant. At low strain rate, however, a flat fracture surface was obtained (Fig. 7(b)), on which slight crack-arrest rather than typical hydrogen-induced cracking feature was found (Fig. 7(d)).

3.2. FCG behavior

Fig. 8 shows the effects of testing temperature on FCG rates obtained at several ΔK values for A533B steel in simulated BWR water. A peak for the FCG rate appeared in the temperature range of 473 to 561 K, which was also typical temperature region for the occurrence of DSA for low-alloy pressure vessel steels [16,17]. This indicated that the FCG rate was enhanced in the DSA temperature region. Brittle-like striations and facets were observed dominantly on the corresponding fracture surfaces (Fig. 9(a)). More typically brittle striated areas were always associated with the MnS inclusions (Fig. 9(b)). Apparent acceleration in the FCG rate has also been reported in the DSA region for low-alloy pressure vessel steels in some previous work. A typical example is shown in Fig. 10, which was replotted from the results of Lee and Kim [14]. An enhanced strain-rate dependence appeared at the loading frequency of 0.05 Hz for A508 Cl.3 steel in high temperature water and the corresponding crack-tip strain rate was in the range of 5×10^{-2} to $1.2\times10^{-1}\%\,s^{-1}$, which was different from the remarkable DSA strain rate (approximate $10^{-2}\%\,s^{-1}$ from Fig. 3) for A533B steel, but was also typical strain-rate region for DSA occurrence for A508 Cl.3 steel [18]. Such a discrepancy in DSA strain-rate range was believed to be due to the different chemical compositions between the two steels. In addition, the authors also observed distinct hydrogen-induced cracking features on the corresponding fatigue fracture surfaces of A508 Cl.3 steel [14]. The above results suggested that both DSA and hydrogen embrittlement were surely involved in the corrosion fatigue process of pressure vessel steels in high temperature water, and their combined actions may significantly aggravate the EAC.

4. Discussion

Much work has been done so far to explain the EAC behavior of materials in high-temperature aqueous environments, mainly consisting of corrosion fatigue

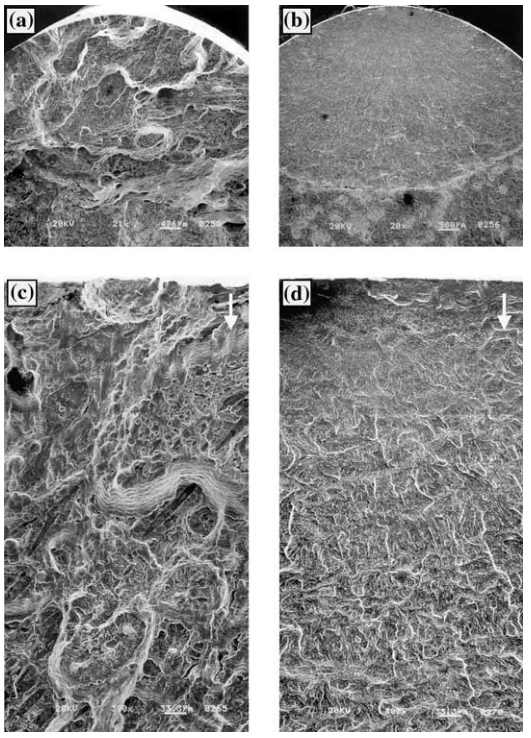

Fig. 7. Fracture surface morphologies at different strain rates (1.0% strain range, arrows: crack growth direction): (a) $0.1\%\,s^{-1}$, (b) $0.001\%\,s^{-1}$, (c) high-magnification morphology of (a), (d) high-magnification morphology of (b).

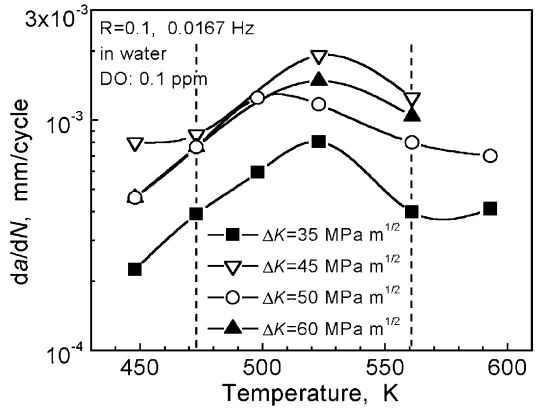

Fig. 8. Effects of temperature on FCG rate of A533B steel in high temperature water.

tests and stress corrosion cracking (SCC) tests [2–16,19–24]. Two basic mechanisms, i.e., hydrogen-induced cracking model and film-rupture/slip-dissolution model, have been generally proposed and accepted. For the former, it was suggested that hydrogen embrittlement facilitated the mechanical separation at the crack tip, which was primarily based on much typically fracto-

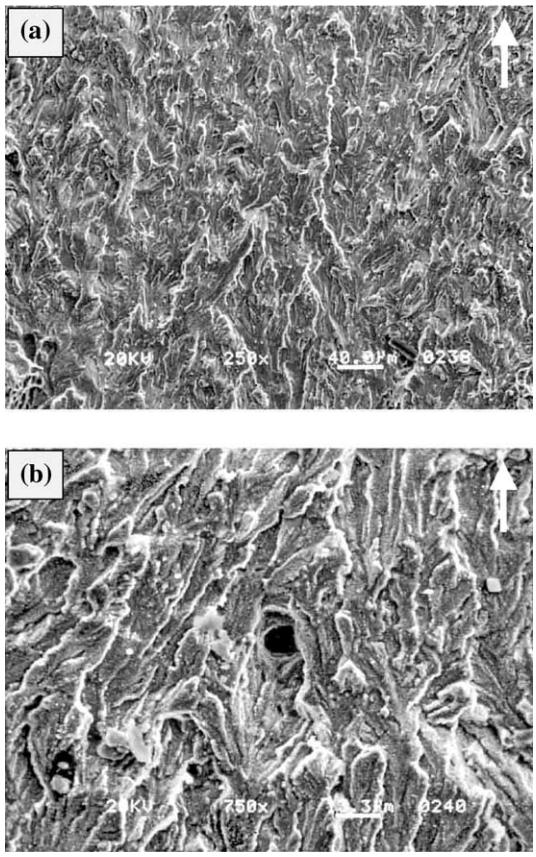

Fig. 9. Typical FCG fracture features of A533B steel in 523 K water, $\Delta K = 45\ \mathrm{MPa\,m^{1/2}}$, arrows: crack growth direction: (a) brittle-like striations and facets, (b) area near an inclusion.

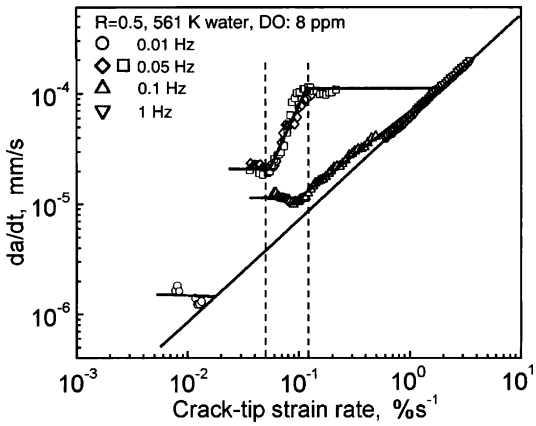

Fig. 10. Dependence of FCG rate of A508 steel on crack-tip strain rate in high temperature water [14].

graphic evidence, such as quasi-cleavage facets or fan-like features extending from sulfide inclusions, terraced morphology produced by linkage of hydrogen-induced

cracks at sulfide/matrix interfaces ahead of the main crack, zig-zag cracking path accompanied by sub-cracks and macrocrack branching, and so on [2,14,16,24]. For the latter, it was believed that anodic dissolution of the bare metal at the crack tip controlled the crack propagation, which was mainly supported by several theoretical prediction models [19–22] and some directly or indirectly associated cracking features, such as surface cracks always showing straight feature and growing as entirely tensile cracks normal to the stress axis throughout the fatigue life, no typical hydrogen-induced cracking morphology on the fracture surfaces, crack arrest along the growth direction, and so on [9,10,25].

Two distinguished cracking morphologies were observed in the present study and were closely dependent on the cyclic strain rate. At relatively high cyclic strain rate ($0.1\%\,s^{-1}$), typical hydrogen-induced cracking features such as tortuous cracks, quasi-cleavage patterns and terraced appearance (Figs. 4(a), 6(a) and 7(c)), were observed frequently. At low strain rate ($0.001\%\,s^{-1}$), however, several cracking features such as entire mode I crack growth behavior and slight crack-arrest (Figs. 4(b), 6(b), (c) and 7(d)), seemed to support the slip-dissolution mechanism. Moreover, it was found that the surface crack density d_c decreased with the increase of cyclic strain rate (Fig. 5(a)) and approximately showed a power-law relationship with the total cyclic tensile time t_t (Fig. 5(b)). If fatigue crack depth was surely proportional to their surface length, final fatigue failure undoubtedly resulted from the integrated contribution of the above surface cracks (especially surface long cracks) to the critical failure crack length a_c. If a_c was assumed to be proportional to d_c, i.e.,

$$a_c \propto d_c. \tag{2}$$

Eq. (1) can be approximately rewritten as

$$a_c = a_0 + k_a \cdot t_t^{0.5}, \tag{3}$$

where constant a_0 can be regarded as the contribution of pre-existed defects or microcracks to final fatigue failure. Eq. (3) indicates a diffusion-controlled crack

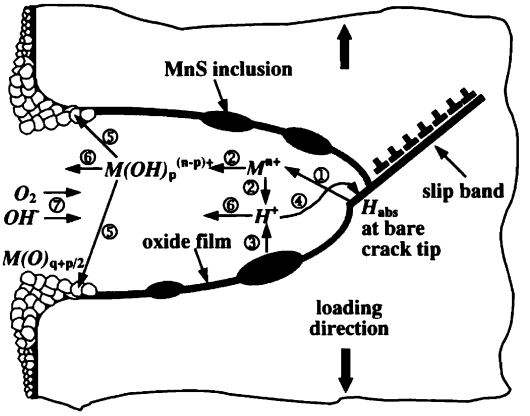

At or near crack tip (DO occluded):

① anodic reaction: $M \rightarrow M^{n+} + ne^-$

② hydrolysis reaction: $M^{n+} + pH_2O \rightarrow M(OH)_p^{(n-p)+} + pH^+$

③ MnS dissolution: $MnS + 4H_2O \rightarrow Mn^{2+} + SO_4^{2-} + 8H^+ + 8e^-$

④ local cathodic reaction: $H^+ + e^- \rightarrow H_{abs} \rightarrow H_{transfer}$

At or near crack mouth (bulk DO):

⑤ local cathodic reaction: $pO_2 + 2pH_2O + 4pe^- \rightarrow 4pOH^-$

Along crack depth direction (mass transfer):

⑥ outward mass transfer from crack tip: H^+, $M(OH)_p^{(n-p)+}$

⑦ inward mass transfer from crack mouth: O_2, OH^-

⑧ reactions: $H^+ + OH^- \rightarrow H_2O$

$$2M(OH)_p^{(n-p)+} + qO_2 + 2(n-p)e^- \rightarrow 2M(O)_{q+\frac{p}{2}} + pH_2O$$

Electrochemistry processes in whole crack system keep balance.

- **strain rate↑(increased)⇒crack open time↓⇒⑥⑦↓⇒DO along crack wall↓ ⇒reaction area for ⑤↓⇒①↓ and ④↑ relatively⇒hydrogen-induced cracking↑**
- **strain rate↓(decreased)⇒crack open time↑⇒⑥⑦↑⇒DO along crack wall↑ ⇒ reaction area for ⑤↑⇒①↑ and ④↓ relatively⇒hydrogen-induced cracking↓ or ⇒⑧↑⇒oxides↑⇒④↓⇒hydrogen-induced cracking↓**
- **MnS inclusions↑⇒③↑⇒④↑ ⇒hydrogen-induced cracking↑**

Fig. 11. Schematic illustration of strain-rate dependent EAC mechanism for pressure vessel steels in high temperature water.

propagation process, which is to some extent consistent with a slip-dissolution controlled process. A similar relationship derived from Ford's slip-dissolution model [19] also appeared in Maiya's phenomenological model for quantitatively describing strain rate, environment and alloy microstructure on the SCC susceptibility [21]. This, at least partly, indicated that the slip-dissolution mechanism played a role in the corrosion fatigue process of the pressure vessel steel in high temperature water.

The present results also suggested that the dominant EAC mechanism for the A533B steel in simulated BWR water changed with decrease of the cyclic strain rate. Fig. 11 outlines a strain-rate dependent EAC mechanism for the pressure vessel steels in high-temperature water environments. It is believed that the cyclic strain rate mainly influences the mass transfer processes (⑥–⑧ in Fig. 11) and local electrochemistry reactions (①–⑤ in Fig. 11) in the crack system, and in turn affects the dominant EAC mechanism.

Special attention should be paid to the effects of MnS inclusions and DSA in the above EAC process, especially in the hydrogen-induced cracking process. As shown in Fig. 11, the dissolution of MnS inclusions exposed to high temperature water changes the local water chemistry in the crack-tip area, in turn accelerates the electrochemical processes in the crack system and enhances local water acidification at or near the crack tip. This may promote the local hydrogen reduction reaction. Furthermore, the matrix/MnS inclusions interfaces ahead of the crack tip are well known as strong traps for hydrogen. So, the MnS inclusions at or near the crack tips may promote the formation and accumulation of active hydrogen. As a result, typical hydrogen-induced cracking features were frequently observed around or near the MnS inclusions (Figs. 7(c) and 9(b)). Both the present results (Figs. 3, 8 and 10) and previous data [3,14,16] showed that the susceptibility of pressure vessel steels to the EAC in high temperature water was closely associated with the DSA behavior of the steels. The role of DSA, especially the combined actions between DSA and hydrogen embrittlement, in enhancing EAC therefore cannot be neglected. Recent studies [26,27] also indicated that a synergism between DSA and hydrogen embrittlement existed in high temperature environments and may promote the EAC. Similar synergism is thus believed to play an important role in the present corrosion fatigue processes, especially for the case of high cyclic or crack-tip strain rate.

5. Conclusions

(1) The cyclic cracking morphologies of A533B steel in simulated BWR water were closely dependent on the strain rate. At a high strain rate, fatigue cracks grew in a tortuous manner and a rough fracture surface was obtained on which hydrogen-induced cracking features were dominant. At a low strain rate, however, fatigue cracks developed in an entirely straight manner and a relatively flat fracture surface was obtained on which slight crack arrest rather than typical hydrogen-induced cracking feature was observed.

(2) The above cracking features in simulated BWR water should be attributed to a change in dominant EAC mechanism from hydrogen-induced cracking mechanism to slip-dissolution mechanism with decrease of the cyclic strain rate.

(3) Both DSA and hydrogen embrittlement were found to be involved in the corrosion fatigue process of low-alloy pressure vessel steels in high temperature water and their combined actions may aggravate the EAC.

(4) A strain-rate dependent EAC mechanism was proposed, in which the strain rate was believed to mainly influence the mass transfer and local electrochemistry processes in the crack system, and MnS inclusions and DSA also played an important role, especially in the hydrogen-induced cracking process.

Acknowledgements

This study was financially supported by the Budget for Nuclear Research of the Ministry of Education, Culture, Sports, Science and Technology, based on the screening and counseling by the Atomic Energy Commission.

References

[1] R. Kilian, A. Roth, Mater. Corros. 53 (2002) 727.
[2] H. Hänninen, K. Torronen, M. Kemppainen, S. Salonen, Corros. Sci. 23 (1983) 663.
[3] Y. Katada, N. Nagata, Corros. Sci. 25 (1985) 693.
[4] F.P. Ford, J. Press. Ves. Technol. 110 (1988) 113.
[5] M. Higuchi, K. Iida, Nucl. Eng. Des. 129 (1991) 293.
[6] N. Nagata, S. Sato, Y. Katada, ISIJ Int. 31 (1991) 106.
[7] H. Kanasaki, M. Hayashi, K. Iida, Y. Asada, ASME PVP 306 (1995) 117.
[8] M. Higuchi, K. Iida, Y. Asada, in: W.A. Van Der Sluys, R.S. Piascik, R. Zawierucha (Eds.), Effects of Strain Rate Change on Fatigue Life of Carbon Steel in High-Temperature Water, ASTM STP, 1298, American Society for Testing and Materials, 1997, p. 216.
[9] D.J. Gavenda, P.R. Luebbers, O.K. Chopra, in: H. Mehta, W. Bamford, S. Bhandari, D. Jones, S. Rahman, G. Wilkowski (Eds.), Crack Initiation and Crack Growth Behavior of Carbon and Low-Alloy Steels, Fatigue and Fracture, vol. 350, American Society of Mechanical Engineers, New York, 1997, p. 243.
[10] O.K. Chopra, W.J. Shack, Nucl. Eng. Des. 184 (1998) 49.
[11] O.K. Chopra, W.J. Shack, J. Press. Ves. Technol. 121 (1999) 49.

[12] A. Hirano, H. Abe, M. Yamamoto, ASME PVP 386 (1999) 201.
[13] M. Higuchi, K. Iida, K. Sakaguchi, ASME PVP 419 (2001) 143.
[14] S.G. Lee, I.S. Kim, J. Press. Ves. Technol. 123 (2001) 173.
[15] G.L. Wire, W.J. Mills, ASME PVP 439 (2002) 151.
[16] J.D. Atkinson, J. Yu, Fat. Fract. Eng. Mater. Struct. 20 (1997) 1.
[17] I.S. Kim, S.S. Kang, Int. J. Press. Ves. Piping 62 (1995) 123.
[18] B.H. Lee, I.S. Kim, J. Nucl. Mater. 226 (1995) 216.
[19] F.P. Ford, ASME PVP 58 (1982) 229.
[20] F.P. Ford, Corros. Sci. 25 (1985) 673.
[21] P.S. Maiya, J. Press. Ves. Technol. 109 (1987) 116.
[22] F.P. Ford, Corrosion 52 (1996) 375.
[23] H. Hänninen, W. Cullen, M. Kemppainen, Corrosion 46 (1990) 563.
[24] M.F. Maday, J. Nucl. Mater. 283–287 (2000) 689.
[25] J.C. Scully, Corros. Sci. 20 (1980) 997.
[26] W.Y. Chu, Y.B. Wang, L.J. Qiao, J. Nucl. Mater. 280 (2000) 250.
[27] X.Q. Wu, I.S. Kim, Mater. Sci. Eng. A 348 (2003) 309.